Self-Reaction of Acetonyl Peroxy Radicals and Their Reaction with Cl Atoms

Mohamed Assali, Christa Fittschen

Self-reaction of Acetonyl Peroxy Radicals and their Reaction with Cl-Atoms

Mohamed Assali and Christa Fittschen*

Université Lille, CNRS, UMR 8522 - PC2A - Physicochimie des Processus de Combustion et de l'Atmosphère, F-59000 Lille, France

*Corresponding author: christa.fittschen@univ-lille.fr

Re-vised version

Submitted to

Journal of Physical Chemistry A

Abstract

The rate constant for the self-reaction of the acetonyl peroxy radicals, $CH_3C(O)CH_2O_2$, has been determined using laser photolysis / continuous wave Cavity Ring Down Spectroscopy (cw-CRDS). $CH_3C(O)CH_2O_2$ radicals have been generated from the reaction of Cl-atoms with $CH_3C(O)CH_3$, and the concentration time profiles of four radicals (HO_2, CH_3O_2, $CH_3C(O)O_2$ and $CH_3C(O)CH_2O_2$) have been determined by cw-CRDS in the near infrared. The rate constant for the self-reaction was found with $k = (5.4 \pm 1.4) \times 10^{-12}$ cm^3s^{-1} in good agreement with a recently published value (Zuraski *et al.*, J Phys Chem A, 124, 8128 (2020)), however the branching ratio for the radical path was found with $\phi_{1b} = (0.6 \pm 0.1)$ well above the recently published value (0.33 ± 0.13). The influence of a fast reaction of Cl-atoms with the $CH_3C(O)CH_2O_2$ radical became evident at some conditions, and therefore this reaction has been investigated in separate experiments. Through simultaneous fitting of all four radical profiles to a complex mechanism, a very fast rate constant of $k = (1.35 \pm 0.8) \times 10^{-10}$ cm^3s^{-1} was found and experimental results could only be reproduced if Cl-atoms would partially react through H-atom abstraction to the formation of the Criegee intermediate with a branching fraction of $\phi_{Criegee} = (0.55 \pm 0.1)$. Modeling the HO_2 concentration-time profiles was only possible if a subsequent reaction of the Criegee intermediate with $CH_3C(O)CH_3$ was included in the mechanism leading to HO_2 formation with a rate constant of $k = (4.5 \pm 2.0) \times 10^{-14}$ cm^3s^{-1}.

Keywords: Peroxy radicals, Criegee intermediate, acetone, laser photolysis, cw-CRDS

Introduction

Acetone is emitted directly by vegetation and is an intermediate in the degradation of biogenic VOCs. It is one of the most abundant volatile organic compounds (VOC) in the atmosphere [1-4] and major degradation paths are through reaction with OH radicals, with a rate constant[5] of $k = 1.8 \times 10^{-13}$ cm^3s^{-1}, and photolysis, leading to an estimated tropospheric lifetime of around 33 and 19 days for reaction with OH and photolysis, respectively[4]. The reaction with OH radicals leads to the formation of the resonantly-stabilized 1-methylvinoxy radicals, $CH_3C(O)CH_2$, also known as acetonyl radical. Vinoxy radicals are known to react with O_2 in equilibrium reactions[6-7], however under tropospheric conditions the equilibrium is on the adduct-side and 1-methylvinoxy leads exclusively to the formation of the acetonyl peroxy radical, $CH_3C(O)CH_2O_2$. In polluted environments, the major fate of this radial is reaction with NO[8], leading to the formation of the acetonoxy radical, $CH_3C(O)CH_2O$, which rapidly

decomposes to formaldehyde, CH_2O, and the acetyl radical, $CH_3C(O)$, no evidence for a reaction of $CH_3C(O)CH_2O$ with O_2 has been found under atmospheric conditions[9]. In pristine environments, self-reaction, cross reactions with other peroxy radicals or reaction with HO_2 becomes the major fate[10].

The self- and cross-reactions of $CH_3C(O)CH_2O_2$ are rather poorly known, the rate constants and branching ratios for the reaction with $CH_3C(O)O_2$, CH_3O_2 and HO_2 have rarely been measured[11-13]. As for the self-reaction, three reaction reaction paths are thought to occur, with two of them leading to stable products, and one (1b) maintaining the radical pool:

$$2\ CH_3C(O)CH_2O_2 \rightarrow CH_3C(O)CH_2OH + CH_3C(O)CHO + O_2 \quad (1a)$$

$$\rightarrow 2\ CH_3C(O)CH_2O + O_2 \quad (1b)$$

$$\rightarrow CH_3C(O)CH_2OOCH_2C(O)CH_3 + O_2 \quad (1c)$$

The rate constant k_1 has been measured three times: In 1990, Cox *et al*.[14] obtained an upper limit of $k_1 \leq 8.3 \times 10^{-12}$ cm^3s^{-1}, deduced from measuring the decay of $CH_3C(O)CH_2O_2$ radicals by UV-absorption without accounting for secondary reactions, which might accelerate the decay of $CH_3C(O)CH_2O_2$ radicals and hence only an upper limit has been given. The result is in good agreement with Bridier *et al*.[11], who obtained by detailed kinetic modeling of UV-absorption profiles a rate constant of $k_1 = (8.0\pm0.2) \times 10^{-12}$ cm^3s^{-1}. In 2020 however, a new determination of k_1 by Zuraski *et al*.[13] is in strong contradiction: they find $k_1 = (4.8 \pm 0.8) \times 10^{-12}$ cm^3s^{-1} using a selective detection of HO_2 and OH radicals by near- and mid-IR spectroscopy and UV-absorption for $CH_3C(O)CH_2O_2$ radicals. The branching ratio has been measured three times for the radical channel (1b) and no agreement is found with values varying between (0.75±0.1)[11], (0.50±0.05)[15] and (0.33±0.13)[13]. The branching fraction for (1c) has been inferred once[16] to $\phi_{1c} = 0.16$ by measuring the rate constant of the product appearance for channel (1c). The currently available literature data, together with the results obtained in this work, are summarized in **Table 1**.

Table 1: Summary of available literature data for the rate constant and the branching ratio of (1)

k_1 / 10^{-12} cm^3s^{-1}	k_{1b} / k_1	k_{1c} / k_1	Reference
≤ 8.3	-	-	Cox *et al.*[14] (1990)
8.0 ± 0.2	0.75 ± 0.1	-	Bridier *et al.*[11] (1993)
4.8 ± 0.8	0.33 ± 0.13	-	Zuraski *et al.*[13] (2020)
-	0.50 ± 0.05	-	Emrich and Warneck[15] (2003)
-	-	0.16	Berndt *et al.*[16] (2018)
8.0 ± 8	0.63 ± 0.2	-	IUPAC[5]
5.4 ± 1.4	0.6 ± 0.1	-	This work

Given the large disagreement between the few literature studies, we present in this work a new determination of the rate constant and branching ratio, based on a different and more selective detection technique: laser photolysis coupled to a detection of the key radicals $CH_3C(O)CH_2O_2$, $CH_3C(O)O_2$, CH_3O_2 and HO_2 by near infrared cw-cavity ring down spectroscopy. As in all previous studies, the radicals have been generated by the reaction of Cl-atoms with $CH_3C(O)CH_3$. During the data evaluation it appeared that the reaction of Cl-atoms with the acetonyl peroxy radical $CH_3C(O)CH_2O_2$ is fast enough to have some influence on the concentration-time profiles under certain experimental conditions. Therefore, the rate constant of this reaction and the branching ratio to the formation of the Criegee intermediate has also been investigated in independent experiments.

Experimental set-up

The experimental set-up has been described in detail several times[17-20], and only a brief description is given here. The reactor consists of a 79 cm long stainless-steel tube with 6 cm inner diameter. The reaction is initiated by excimer laser photolysis (Lambda Physik LPX 202i), whereby the beam is delimited to a width of 2 cm. Two cw-CRDS paths are installed in a small angle with respect to the photolysis laser, leading to an overlap between photolyzed volume and probe beam of 28.8 cm. Ring down times are measured in a time-resolved way with respect to the photolysis pulse and allow obtaining time resolved concentration profiles of radicals. Ring-down events occur randomly and are collected over typically 30 – 50 photolysis shots in order to obtain a good description of the absorption behavior, see for example Figure 1: each dot corresponds to a ring-down event having occurred randomly with respect to the photolysis pulse. Ring-down times from events having occurred before the photolysis pulse (up to -500 ms) are all averaged and used to convert ring-down times after the laser pulse into absorption coefficients α.

The cw-CRDS absorption set-ups runs in the near infrared range and the two paths have been equipped with highly reflective mirrors efficient in different wavelength ranges, allowing to cover ≈1400 – 1600 nm on one path and ≈1300 – 1400 nm on the other path. Three different distributed feedback (DFB) lasers are used for the detection of the species ($CH_3C(O)O_2$: Alcatel A1905LMI 3CN004 1 0CR, 6497±18 cm^{-1}, HO_2: NEL NLK1E5GAAA, 6629±17 cm^{-1}, on CRDS path 1, CH_3O_2 and $CH_3C(O)CH_2O_2$: NEL NLK1B5EAAA, 7480±20 cm^{-1} on CRDS path 2). Typical ring-down times in the empty cavity can be up to τ_0 = 100 µs with very clean mirrors and good alignment. With an estimated measurable decrease in ring-down time of 1µs (*i.e.* τ = 99µs) the detection limits in 100 Torr O_2 vary from ~4×10^{10} cm^{-3} for HO_2

to ~1.5×10^{12} cm^{-3} for $CH_3C(O)CH_2O_2$. More details on the experimental set-up are given in earlier papers[17-20] and more details on the radical detection and quantification will be given further down.

Laser photolysis of Cl_2 at 351 nm at a repetition rate of 0.3 Hz has been used in all experiments to generate radicals:

$$Cl_2 + h\nu_{351nm} \rightarrow 2\ Cl \qquad (2)$$

$$Cl + CH_3C(O)CH_3 \rightarrow CH_3C(O)CH_2 + HCl \qquad (3)$$

The rate constants of (3) is k_3 = 2.1 × 10^{-12} cm^3s^{-1} [5], leading with typical $CH_3C(O)CH_3$ concentration between (0.5 – 7.2) × 10^{16} cm^{-3} to pseudo-first-order rate constants of k_3^{1st}= (0.1 – 1.5) × 10^5 s^{-1}. All experiments have been carried at a total pressure of 100 Torr O_2, leading to

$$CH_3C(O)CH_2 + O_2 \rightarrow CH_3C(O)CH_2O_2 \qquad (4)$$

With k_4 =1.2 × 10^{-12} $cm^3\ s^{-1}$ [6], reaction (4) is completed within a few µs and is considered as the only fate of the $CH_3C(O)CH_2$ radical.

Rate constants and branching ratios for the two title reactions have been deduced by simultaneously adjusting the concentration-time profiles of the 4 key radicals ($CH_3C(O)CH_2O_2$, $CH_3C(O)O_2$, CH_3O_2 and HO_2), obtained under different initial concentrations, to a complex model (given in Table 3).

Typical concentrations were: Cl_2 = (4 - 9) × 10^{15} cm^{-3} , $CH_3C(O)CH_3$ = (0.5 – 7.2) × 10^{16} cm^{-3}. O_2 (Alphagaz 2, Air Liquide) was used without further purification. Concentrations have been calculated from pressure measurements (Baratron, 1000 Torr) and calibrated flowmeters (Tylan and Bronkhorst).

Results and discussion

Detection of radicals

The self-reaction of $CH_3C(O)CH_2O_2$ is thought to have three reaction paths, whereof (1a) and (1c) lead to stable products, not influencing the kinetic measurements of our experiments, while path (1b) leads to formation of radicals through rapid decomposition of the initially formed alkoxy radical:

$$CH_3C(O)CH_2O \rightarrow CH_3CO + CH_2O \qquad (5)$$

which in the presence of O_2 will rapidly lead to formation of the acetyl peroxy radical, $CH_3C(O)O_2$, as well as to the formation of a few percent of OH and HO_2 radicals[21-22]:

$$CH_3CO + O_2 \rightarrow CH_3C(O)O_2 \qquad (6a)$$

$$CH_3CO + O_2 \rightarrow \text{products} + OH\ /\ HO_2 \qquad (6b)$$

The $CH_3C(O)CH_2O_2$ decay will subsequently be perturbed by complex secondary chemistry:

$$CH_3C(O)CH_2O_2 + CH_3C(O)O_2 \rightarrow CH_3C(O)OH + CH_3C(O)CHO + O_2 \quad (7a)$$

$$\rightarrow CH_3C(O)O + CH_3C(O)CH_2O + O_2 \quad (7b)$$

with an estimated rate constant[11] of $k_7 = (5.0 \pm 2.0) \times 10^{-12}$ $cm^3\,s^{-1}$ and a branching ratio of $\phi_7 = (0.5 \pm 0.2)$[12]. The product of (7b), $CH_3C(O)CH_2O$, will rapidly decompose to regenerate the $CH_3C(O)O_2$ radicals while the other product, $CH_3C(O)O$, rapidly decomposes and leads to formation of CH_3O_2 radicals. These radicals will induce further secondary chemistry:

$$CH_3C(O)CH_2O_2 + CH_3O_2 \rightarrow CH_3C(O)CH_2O + CH_3O + O_2 \quad (8a)$$

$$\rightarrow \text{stable products} \quad (8b)$$

Products from (8a) will rapidly lead to formation of $CH_3C(O)O_2$ and HO_2 radicals, with the latter one reacting also with $CH_3C(O)CH_2O_2$ radicals:

$$CH_3C(O)CH_2O_2 + HO_2 \rightarrow CH_3C(O)CH_2O + OH + O_2 \quad (9a)$$

$$\rightarrow \text{stable products} \quad (9b)$$

Concomitantly, the self-reaction of $CH_3C(O)O_2$ radicals (10) will also leads to formation of CH_3O_2 radicals, while their cross reaction with CH_3O_2 (11) leads to more HO_2 and their cross-reaction with HO_2 leads to more CH_3O_2 and also to OH (12). Simultaneous self-reaction of CH_3O_2 (13), its cross reaction with HO_2 (14) as well as the self-reaction of HO_2 (15) further complicates the system. In order to better quantify this complex reaction system induced by the self-reaction (1) and with the goal of measuring k_1, it is therefore highly desirable to selectively detect all these key radicals. Here, we determined the concentration-time profiles of the four main radicals: HO_2, CH_3O_2, $CH_3C(O)O_2$ and $CH_3C(O)CH_2O_2$ by using cw-CRDS in the near IR.

- ***HO_2*** has been detected in the $2\nu_1$ transition at 6638.20 cm^{-1}. The spectrum of this radical has been measured several times[23-29] and is very structured. A highly selective quantification can be obtained by removing the contribution of possible broadband absorbers ($CH_3C(O)O_2$ in this system[21]) by measuring profiles on top of the absorption line (red circles in **Figure 1a**) and at a wavelength just next to it (black circles in **Figure 1a**): HO_2 profiles are then obtained by subtracting online – offline (red dots in **Figure 1a**). The absorption cross sections of this transition has been determined several times and a cross section of $\sigma_{HO_2,\,100\,Torr} = (2.0 \pm 0.3) \times 10^{-19}$ cm^2 is used in this work.
- ***$CH_3C(O)O_2$*** is quantified in the $\tilde{A}$-$\tilde{X}$ electronic transition at 6497.94 cm^{-1} (blue dots on right y-scale in **Figure 1b**) with an absorption cross section of $\sigma_{CH_3C(O)O_2} = 3.3 \times 10^{-20}$ cm^2 [30]. Even though the

transition is less structured than the HO_2 spectrum, absorption time profiles at different wavelengths always lead to identical shapes: in **Figure 1b** is shown again the offline HO_2 signal from **Figure 1a**, now scaled on the left y-axis to overlay with the $CH_3C(O)O_2$ signal. These identical shapes at distant wavelengths confirms (a) that the detection of $CH_3C(O)O_2$ radicals at 6497.94 cm^{-1} in this reaction system is selective and (b) that the HO_2 offline signal is due to $CH_3C(O)O_2$ radicals.

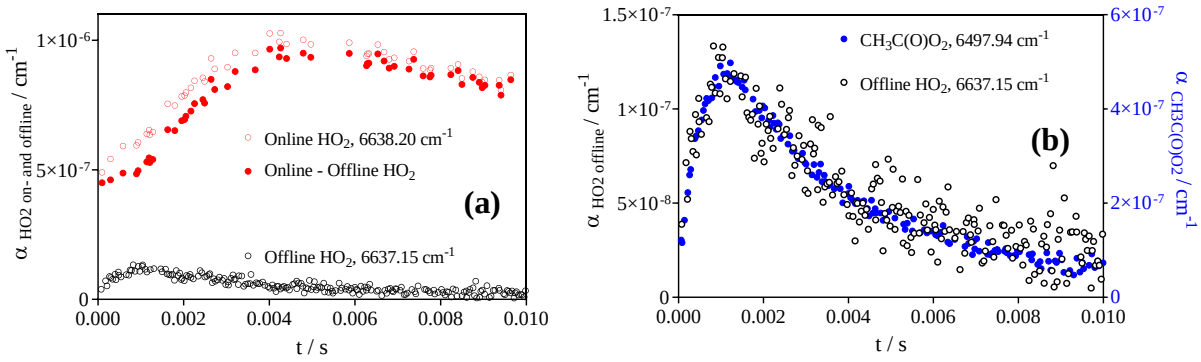

Figure 1 : Absorption time profiles for HO_2 and $CH_3C(O)O_2$. Both graphs : black circles is offline HO_2 measured at 6637.15 cm^{-1}. Graph a: Online HO_2 measured at 6638.2 cm^{-1} (red circle), red dots is difference between online and offline. Graph b: Online $CH_3C(O)O_2$ (blue dots on right y-axis).

- ***$CH_3C(O)CH_2O_2$*** has to our knowledge never been detected in the near IR range. The absorption spectrum of the electronic transition of the $CH_3C(O)CH_2O_2$ radical can reasonably well be expected in the wavelength range of other alkyl peroxy radicals, and therefore we have tentatively tested for absorption of this radicals in the wavelength range accessible with the DFB laser used for the CH_3O_2 radical (NEL NLK1B5EAAA, 7480±20 cm^{-1}). The absorption coefficient at 7491.31 cm^{-1} has been measured following the 351 nm photolysis of Cl_2 in presence of $CH_3C(O)CH_3$ and 100 Torr O_2, leading through the reaction sequence (2) to (4) to rapid formation of $CH_3C(O)CH_2O_2$. The absolute absorption cross section has then been determined in back-to-back experiments by replacing $CH_3C(O)CH_3$ with CH_3OH, which leads to rapid formation of HO_2, which in turn can be quantified (see above). This way, the initial Cl-atom concentration is determined, and under the hypothesis, that in both experiments all Cl-atoms are converted into either $CH_3C(O)CH_2O_2$ or HO_2, the absorption cross section of $CH_3C(O)CH_2O_2$ is then determined relative to the HO_2 absorption cross section. The radicals decay mostly by self-reaction, therefore a linear regression of a plot of $1/\alpha = f(t)$ allows a more reliable extrapolation to $\alpha_{t=0s}$, the absorption coefficient just after the photolysis pulse[26]. **Figure 2** shows a typical example with 4 different Cl-concentrations: graph (a) shows a plot of $1/\alpha_{6638,58\ cm^{-1}} = f(t)$ for the experiments with CH_3OH, graph (b) shows $1/\alpha_{7491.31\ cm^{-1}} = f(t)$ for the same Cl-concentration in presence of $CH_3C(O)CH_3$. In graph (c) the absorption coefficient at 7491.31 cm^{-1} has been plotted against the concentration of HO_2, whereby the concentration has been obtained from $\alpha_{6638,58\ cm^{-1}}$ converted to $[HO_2]$ by using $\sigma = 2.1 \times 10^{-20}$ cm^2. This line has been used

for quantification of Cl-atoms only, because the line at 6638.20 cm^{-1}, used for all other measurements, is too strong and would lead to saturation under the high Cl-atom concentrations. Linear regression of these data leads to an absorption cross section of the $CH_3C(O)CH_2O_2$ radical at 7491.31 cm^{-1} of $\sigma = (6.5\pm0.5) \times 10^{-21}$ cm^2. Experiments at a different wavelength (7489.16 cm^{-1}) resulted in an identical absorption cross section, indicating a broad, non-structured absorption feature of $CH_3C(O)CH_2O_2$ in this wavelength range. Measuring the absorption spectrum of this radical in a larger wavelength range is certainly desirable to identify possible structures, unfortunately currently we do not have light sources that would allow such measurements.

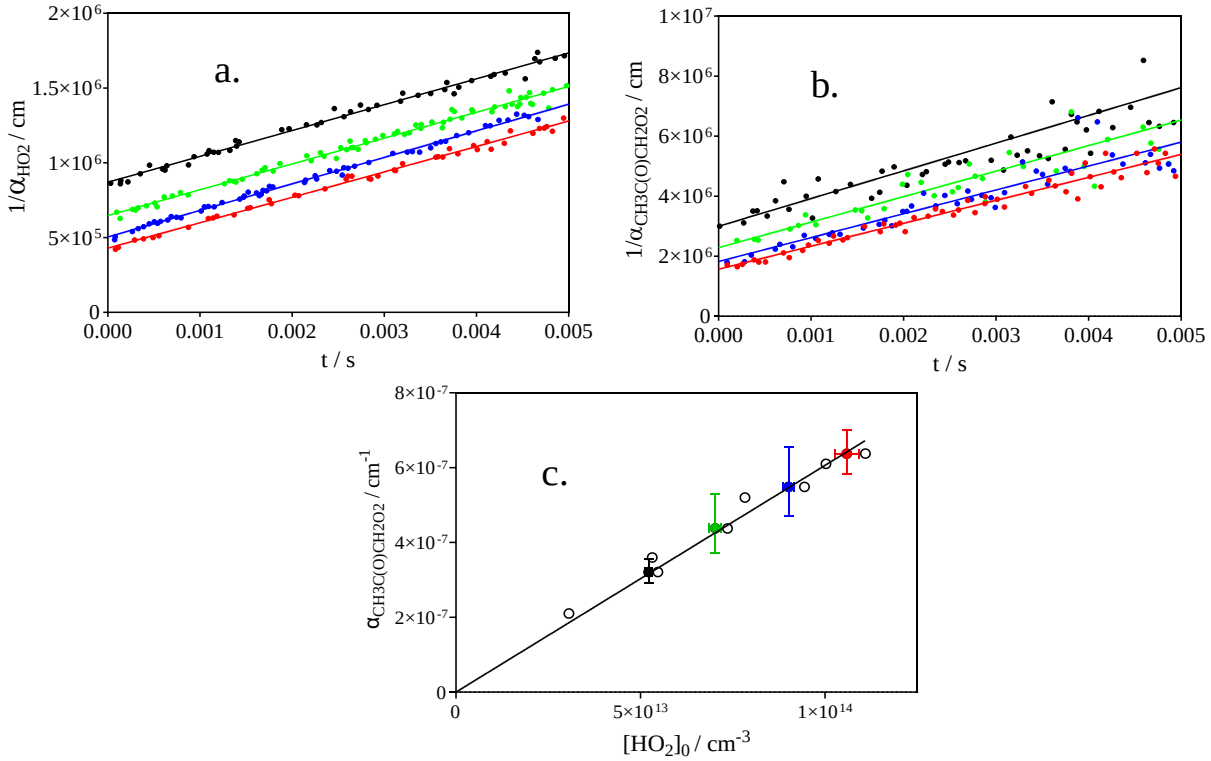

Figure 2 : Absorption time profiles for HO_2 (graph a) and $CH_3C(O)CH_2O_2$ (graph b), expressed as $1/\alpha = f(t)$ at 4 different initial Cl_2 concentration (in 10^{15} cm^{-3}) : 4.0 (black), 5.7 (green), 7.3 (blue) and 9.0 (red) with $[CH_3C(O)CH_3] = 7.2 \times 10^{16}$ cm^{-3} at 100 Torr O_2. Graph c. shows $\alpha_{7491.31\ cm^{-1},\ t=0s}$ from graph b. as a function of $[HO_2]_{t=0s}$ from graph a., open circle are other data sets. Linear regression leads to $\sigma = (6.5\pm0.2) \times 10^{-21}$ cm^2. Error bars are statistical 95% confidence interval.

- ***CH_3O_2*** has been quantified in the $\tilde{A}$-$\tilde{X}$ transition at 7489.16 cm^{-1}. The absorption spectrum of CH_3O_2 has some maxima on a broad background[31], similar to the one of $CH_3C(O)O_2$. Therefore, it is not straightforward to reach selectivity through online and offline measurements. In our recent work on the $CH_3C(O)O_2$ self-reaction we have shown, that the CH_3O_2 is not selective anymore because absorption-time profiles registered on and off the peak wavelength clearly do not have the same shape. From different experiments it was concluded that $CH_3C(O)O_2$ is still absorbing in the CH_3O_2 wavelength range[21]. This has also to be considered in this work, because $CH_3C(O)O_2$ is a reaction

product of the $CH_3C(O)CH_2O_2$ self-reaction. In the present work, the situation is even more complex, as it has just been shown that the $CH_3C(O)CH_2O_2$ radical also absorbs in this wavelength range. Therefore, in this reaction system the absorbance around 7489.16 cm^{-1} needs to be expressed as the sum of the 3 radicals CH_3O_2, $CH_3C(O)O_2$ and $CH_3C(O)CH_2O_2$ with absorption cross sections such as given in **Table 2**.

Table 2: Absorption cross sections at 100 Torr O_2 of HO_2, CH_3O_2, $CH_3C(O)O_2$ and $CH_3C(O)CH_2O_2$

	σ / cm^2 at 7491.31 cm^{-1}	σ / cm^2 at 7489.16 cm^{-1}	σ / cm^2 at 6638.20 cm^{-1}	σ / cm^2 at 6638.58 cm^{-1}	σ / cm^2 at 6497.94 cm^{-1}
HO_2	-	-	2.0×10^{-19}	2.1×10^{-20}	-
CH_3O_2	6.1×10^{-21}	2.4×10^{-20}	-		-
$CH_3C(O)O_2$	4.3×10^{-21}	4.3×10^{-21}	8.3×10^{-21}		3.3×10^{-20}
$CH_3C(O)CH_2O_2$	6.5×10^{-21}	6.5×10^{-21}	-		

Figure 3 shows two absorption time profiles, measured under the same experimental conditions, with graph (a) showing the profile obtained at the CH_3O_2 peak wavelength, while graph (b) shows the profile obtained off the main CH_3O_2 absorption feature. It can be seen that both profiles show the same absorbance at short reaction times ($\alpha_{t=0s} \approx 6\times10^{-7}$ cm^{-1}), while the evolution of the shape at longer reaction times is very different at both wavelengths. The only radical present in sizeable concentrations just after the photolysis pulse is $CH_3C(O)CH_2O_2$, and hence the initial absorption can be assigned to this radical. The colored lines in **Figure 3** indicate the absorption time profiles such as obtained from modeling (see further down), and the black line represents the sum of the absorption of the three species. In the first few ms, the shape of graph (a) is dominated by the formation of CH_3O_2 radicals (green) with the absorption cross section of CH_3O_2 being nearly 4 times larger than the absorption cross section of $CH_3C(O)CH_2O_2$, while graph (b) is dominated by the decay of the $CH_3C(O)CH_2O_2$ radical (red) because at this wavelength the absorption cross section of both radicals are comparable and the concentration of $CH_3C(O)CH_2O_2$ is high compared to CH_3O_2. The absorbance due to $CH_3C(O)O_2$ (blue) is only minor at both wavelength due to the small absorption cross section together with the relatively low concentration of this radical. Moreover, its absorbance can be accurately accounted for by simultaneous and selective measurement of this radical at its peak wavelength 6497.94 cm^{-1}. From this example it can be seen that, even though full selectivity cannot be achieved, simultaneous simulation of absorption time-profiles at three wavelengths allows to well-describe the profiles of both radicals, CH_3O_2 and $CH_3C(O)CH_2O_2$.

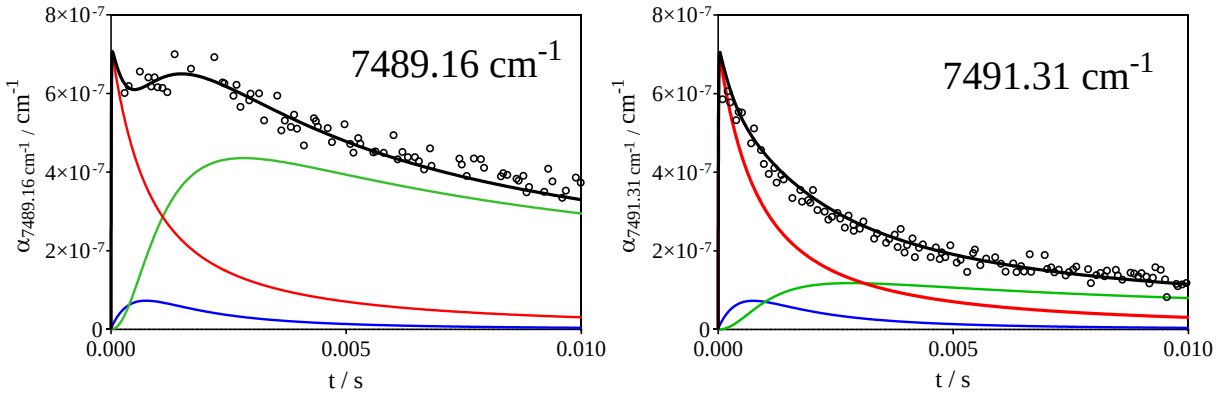

Figure 3: Absorption-time profiles measured at 7489.16 cm^{-1} (left, "online" CH_3O_2) and at 7491.31 cm^{-1} (right, "offline" CH_3O_2) following photolysis of $[Cl_2]$ = 7.3×10^{15} cm^{-3} in presence of $[CH_3C(O)CH_3]$ = 7.2×10^{16} cm^{-3} in 100 Torr of O_2. Full lines represent modelled absorption time profiles (concentration time profiles obtained by using the model in **Table 3**, multiplied with the absorption cross sections from **Table 2**) for $CH_3C(O)O_2$ (blue), CH_3O_2 (green), $CH_3C(O)CH_2O_2$ (red) and the sum of the three species profiles (black).

As a conclusion from this paragraph it can be summarized that the concentrations of the four key radicals involved in this system can be obtained as follows:

- $CH_3C(O)O_2$ at 6497.94 cm^{-1} using $\sigma = 3.3\times10^{-20}$ cm^2
- HO_2 at 6638.20 cm^{-1} using $\sigma = 2.0\times10^{-19}$ cm^2 after subtraction of offline measurements, carried out at the same condition
- CH_3O_2 at 7489.16 cm^{-1} using $\sigma = 2.4\times10^{-20}$ cm^2 and taking into account minor contributions from $CH_3C(O)CH_2O_2$ ($\sigma = 6.5\times10^{-21}$ cm^2) and $CH_3C(O)O_2$ ($\sigma = 4.3\times10^{-21}$ cm^2). For practical purposes, absorption-time profiles at 7489.16 cm^{-1} are converted to concentration-time profiles using $\sigma=2.4\times10^{-20}$ cm^2 and the profiles are then expressed as sum of

  $$[CH_3O_2]_{sum} = [CH_3O_2] + 0.18 \times [CH_3C(O)O_2] + 0.27 \times [CH_3C(O)CH_2O_2] \quad (16)$$

  with $0.18 = 4.3\times10^{-21} / 2.4\times10^{-20}$ and $0.27 = 6.5\times10^{-21} / 2.4\times10^{-20}$ (see Figures 4, 6, 7 and 8).
- $CH_3C(O)CH_2O_2$ at 7491.31 cm^{-1} using $\sigma=6.5\times10^{-21}$ cm^2 and taking into account minor contributions from CH_3O_2 ($\sigma = 6.1\times10^{-21}$ cm^2) and $CH_3C(O)O_2$ ($\sigma = 4.3\times10^{-21}$ cm^2). For practical purposes, absorption-time profiles at 7491.31 cm^{-1} are converted to concentration-time profiles using $\sigma=6.5\times10^{-21}$ cm^2 and the profiles are then expressed as sum of

  $$[CH_3C(O)CH_2O_2]_{sum} = [CH_3C(O)CH_2O_2] + 0.66 \times [CH_3C(O)O_2] + 0.94 \times [CH_3O_2] \quad (17)$$

  with $0.66 = 4.3\times10^{-21} / 6.5\times10^{-21}$ and $0.94 = 6.1\times10^{-21} / 6.5\times10^{-21}$ (see Figures 4, 6, 7 and 8).

Reaction of Cl-atoms with $CH_3C(O)CH_2O_2$

The rate constant of the reaction of $CH_3C(O)CH_3$ with Cl-atoms is with $k_3 = 2.17 \times 10^{-12}$ cm^3 s^{-1} [32] not very fast and is leading with our typical $CH_3C(O)CH_3$ concentrations between $(0.5 – 7.2) \times 10^{16}$ cm^{-3} to pseudo-first-order rate constants of $k_3^{1st} = (0.1 – 1.5) \times 10^5$ s^{-1}. The consecutive formation of peroxy radicals in 100 Torr O_2 is more than 10 times faster[6] and can be considered instantaneous. The reaction of Cl-atoms with the $CH_3C(O)CH_2O_2$ radical has to our knowledge never been measured, but the comparable reaction between Cl-atoms and CH_3O_2 radicals has been found very fast with rate constants up to 2×10^{-10} cm^3 s^{-1} [33-34]. Similar to CH_3O_2, the reaction can be expected to proceed by an initial addition of the Cl-atom to the oxygen atom and to continue to react over submerged barriers[35]. By comparison with CH_3O_2, the following three reaction paths can then be expected for the reaction of Cl-atoms with the $CH_3C(O)CH_2O_2$:

$$CH_3C(O)CH_2O_2 + Cl \rightarrow CH_3C(O)CH_2O + ClO \quad (18a)$$

$$\rightarrow CH_3C(O)CHO_2 + HCl \quad (18b)$$

$$\rightarrow CH_3C(O)CHO + HOCl \quad (18c)$$

The possible abstraction of an H-atom from the remaining CH_3-group can be neglected, because the rate constant for (18) has been found around 100 times faster than the rate constant for the reaction of Cl-atoms with $CH_3C(O)CH_3$: it is not likely that replacement of an H-atom in γ-position by O_2 leads to a strong increase of the rate constant.

Such a fast reaction could play some role in the present reaction system: due to the fact that the self-reaction of $CH_3C(O)CH_2O_2$ is not too fast (see below), initial Cl-atom concentrations were typically around 10^{14} cm^{-3} in order to induce a sizeable reactivity on the tens of millisecond timescale. Under such conditions, the reaction of Cl-atoms with $CH_3C(O)CH_2O_2$ might become competitive with (1). We have therefore in a first step investigated this reaction by carrying out experiments that promote this reaction: high Cl-atom concentration next to low $CH_3C(O)CH_3$ concentration.

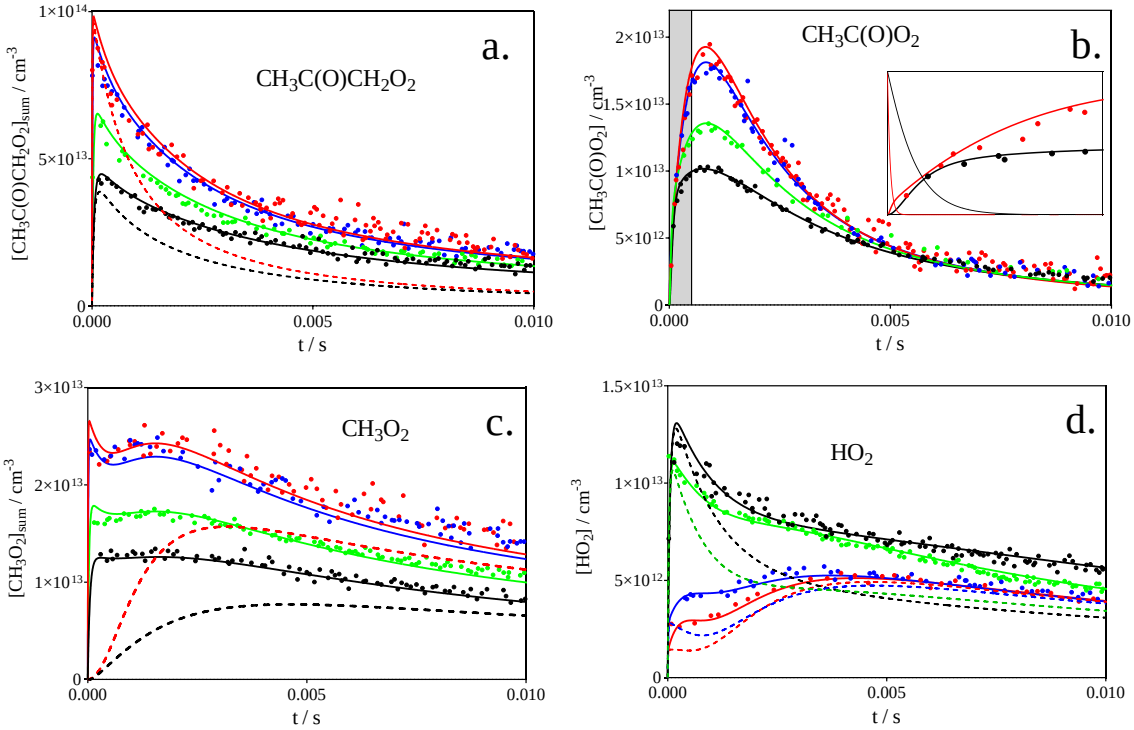

Figure 4: Absorption-time profiles for all 4 radicals: [Cl] = 1.1 × 10^{14} cm^{-3}, [$CH_3C(O)CH_3$] = 7.2, 3.5, 1.2, 0.41 × 10^{16} cm^{-3} and [CH_2O] = 4.2 × 10^{13} cm^{-3} for red, blue, green and black symbols, respectively. Full lines are obtained using the model in **Table 3**, for CH_3O_2 and $CH_3C(O)CH_2O_2$ data points and full lines are expressed corresponding to (16) and (17), respectively. Insert in graph b. is a zoom on grey-shaded area for highest and lowest Cl-atom concentration, decreasing curves are simulated Cl-atom concentrations. Dashed lines in graph a. and c. show contribution of $CH_3C(O)CH_2O_2$ and CH_3O_2 radicals to the total signal for the highest and lowest $CH_3C(O)CH_3$ concentration. Dashed line in graph d. shows HO_2 signal without contribution of (19)

Figure 4 shows the profiles of all 4 species from the reaction of $[Cl]_0$ = 1.1 × 10^{14} cm^{-3} in presence of 4 different $CH_3C(O)CH_3$ concentrations, decreasing from 7.2 × 10^{16} cm^{-3} (red) to 4.1 × 10^{15} cm^{-3} (black). The full lines describe the output of the model given in **Table 3**.

In graph (4a) it can be seen that the initial $CH_3C(O)CH_2O_2$ concentration decreases with decreasing $CH_3C(O)CH_3$: this is due to an increased competition for Cl-atoms between $CH_3C(O)CH_3$ and $CH_3C(O)CH_2O_2$. For the two highest $CH_3C(O)CH_3$ concentration the impact is barely visible, *i.e.* the $CH_3C(O)CH_3$ concentration is high enough to be the major fate for Cl-atoms. However for the two lowest $CH_3C(O)CH_3$ concentrations the increasing influence of (18) is clearly visible. This decrease in initial $CH_3C(O)CH_2O_2$ concentration with decreasing $CH_3C(O)CH_3$ is very sensitive to the overall rate constant of (18) and through simultaneous modelling of the concentration time profiles of all radicals an overall rate constant of k_{18} = (1.35 ± 0.2) ×10^{-10} cm^{3}s^{-1} has been obtained.

Graph (4b) shows the $CH_3C(O)O_2$ profiles: while this radical is the products of path (1b) of the self-reaction of $CH_3C(O)CH_2O_2$, it is also the product of path (8a), (9a) and of the reaction of Cl-atoms with

$CH_3C(O)CH_2O_2$ (18a). The insert of graph (4b) shows a zoom for the first 500 µs for the highest and lowest $CH_3C(O)CH_3$ concentration, together with the simulated Cl-atom decays (a secondary y-axis applies for Cl-atoms, starting at 1.1×10^{14} cm^{-3}). It can be seen that for the highest $CH_3C(O)CH_3$ concentration the Cl-atoms have decayed well before a noticeable rise of the $CH_3C(O)O_2$ concentration: under these conditions, reaction (1b) is the main source for $CH_3C(O)O_2$. For the lowest $CH_3C(O)CH_3$ concentration, the major rise of $CH_3C(O)O_2$ occurs during the Cl-atom decay, and it can be concluded that under these conditions path (18a) is the major source, while path (1b) is less important due to the lower $CH_3C(O)CH_2O_2$ concentration. The subsequent decay is due to cross-reactions with the other radicals. Simulating these profiles (together with the HO_2 profiles) has a high sensitivity to the branching fraction of (18a) and best results were obtained with a branching fraction of $\phi_{18a} = 0.45$. Because path (18c) is decreasing the overall radical concentration, the observed profiles of all four species could only be reproduced with a negligible branching fraction and is hence considered $\phi_{18c} = 0$. This is in agreement with experiments on CH_3O_2 and $C_2H_5O_2$, where the products corresponding to this reaction path, have never been observed. From these considerations we predict the formation of the Criegee intermediate (18b) to be the major path for the reaction of Cl-atoms with $CH_3C(O)CH_2O_2$ with a branching fraction of $\phi_{18b} = (0.55\pm0.1)$. The uncertainty for the branching fraction has been estimated from using models with different ratios of k_{18a}/k_{18b}, and an example is given in Figure S1.

Graph (4c) shows the CH_3O_2 signal. For this radical, the major source is the cross reaction between $CH_3C(O)CH_2O_2$ and $CH_3C(O)O_2$ radicals, (R18) does not contribute to this radical concentration. From the modelled CH_3O_2 profiles for the highest and lowest $CH_3C(O)CH_3$ concentration (dashed lines) it can be seen that CH_3O_2 radicals are formed delayed, the time necessary to build up the $CH_3C(O)O_2$ concentration. The difference in absolute concentration is then due to the difference in $CH_3C(O)CH_2O_2$ concentration.

Graph (4d) shows the HO_2 concentration time profiles which turned out to be very sensitive to (18). Very rapid HO_2 formation is observed under all conditions, and a strong increase of this concentration occurs with decreasing $CH_3C(O)CH_3$ concentration. In absence of (18), HO_2 is formed only from secondary reactions involving products of initial reactions, and therefore this rapid HO_2 formation was a surprise. However, test experiments using different photolysis repetition rates confirmed a suspicion, that HO_2 is formed from the fast reaction of Cl-atoms with residual CH_2O:

$$Cl + CH_2O \rightarrow HCl + HCO \xrightarrow{O_2} CO + HO_2 \qquad (19)$$

with $k_{19} = 7.2\times10^{-11}$ cm^3s^{-1} around 35 times faster than k_3, and therefore even small concentrations of CH_2O can compete with $CH_3C(O)CH_3$. CH_2O is one of the final products of (1b), but also a product of other cross reactions in this system. The gas mixture is renewed roughly every 2 laser shots, with an

additional refreshment of the gas mixture through diffusion out of the photolyzed volume (less than 10% of the volume is photolyzed at each shot due to the cell volume being much larger than the photolysed volume). Some residual CH_2O possibly remains in the observation volume and is the major HO_2 source at very short reaction times, with the concentration increasing with decreasing $CH_3C(O)CH_3$ concentrations. Therefore, a variable initial CH_2O concentration (typically $1 – 4 \times 10^{13}$ cm^{-3}) has always been added to the model such as to adjust the initial HO_2 concentration. As other carbonyl compounds, $CH_3C(O)CH_3$ reacts in an equilibrium reaction with HO_2 radicals: a recent measurement[13] finds an equilibrium constant of $K_c = (1.4\pm0.8) \times 10^{-18}$ cm^{-3} $molecule^{-1}$, which is around 10 and 500 times smaller than the corresponding equilibrium constants for CH_3CHO and CH_2O[36]. The establishment of the equilibrium is rapid, thus resulting in an overall reduced HO_2 concentration profile. Adding the equilibrium reaction from Zuraski et al. to the model results in an HO_2 decrease between 1 – 12% for the lowest to the highest $CH_3C(O)CH_3$ concentration and this decrease can be compensated for by a slight increase of the residual CH_2O concentration, without any effect on the rate constant of the title reactions.

Following the rapid HO_2 formation initiated by (19), the subsequent evolution of the HO_2 concentration is governed by its formation through some cross- and self-reactions (8a, 11a and 13a) and its consumption through other cross- and self-reactions (9, 12, 14 and 15). For this reason, the concentrations of all four HO_2 traces in **Figure 4** converge to similar concentrations at longer reaction times, given by the equilibrium between formation and consumption and depending on the overall radical concentration. However, in a first try it was found impossible to simulate the approach of the HO_2 profiles to this equilibrium in the first few ms, the result is shown as dashed lines in **Figure 4d**: for high $CH_3C(O)CH_3$ concentration (red), some rapid HO_2 formation was missing, while for low $CH_3C(O)CH_3$ concentration (black) the decay was too fast and also the concentrations decayed to too low levels. The overall radical concentration in this case is low due to a non-negligible fraction of Cl-atoms reacting through (18), so cross reactions between the different peroxy radicals are too slow to maintain the HO_2 concentration up to the observed level. Therefore, different reactions leading to formation of HO_2 following (18) were tested in the model.

The product of (18a) will decompose to CH_2O and, after addition of O_2, to $CH_3C(O)O_2$, and thus leads only through subsequent cross reactions to HO_2 formation. Pathway (18c) leads to stable reaction products only and cannot be the candidate. Therefore, the participation of the Criegee intermediate, reaction product of (18b), was considered as an additional HO_2 source. **Figure 5** shows again the HO_2 profiles from **Figure 4d**, now using the unimolecular decomposition of the $CH_3C(O)CHO_2$ radical as source of HO_2 radicals:

$$CH_3C(O)CHO_2 \rightarrow \rightarrow \rightarrow HO_2 \qquad (20)$$

Such a model does not allow to reproduce the HO_2 profiles for all concentrations: a low rate constant (k_{20} = 250 s^{-1}, graph a.) allows reproducing the profile obtained with low $CH_3C(O)CH_3$ concentration (black), but still underpredicts the signal at high $CH_3C(O)CH_3$ concentration (red). The red profile on the other hand can be well adjusted using k_{20} = 3000s^{-1} (graph b.), but then the black profile is strongly overpredicted. Therefore, the unimolecular decomposition of $CH_3C(O)CHO_2$ doesn't seem to play any major role for the HO_2 profiles in our system. This is in good agreement with Vereecken *et al*.[37-38], who developed a SAR for unimolecular reactions of Criegee intermediates.They predict as the preferred channel for the $CH_3C(O)CHO_2$ radical the formation of dioxirane with a rate constant of 19 and 0.06 s^{-1} for the Z- and E-isomer, respectively. Such rate constants lead to lifetimes of ≈50 ms and ≈15 s, respectively, while the observed HO_2 formation in our experiments occur in a few ms.

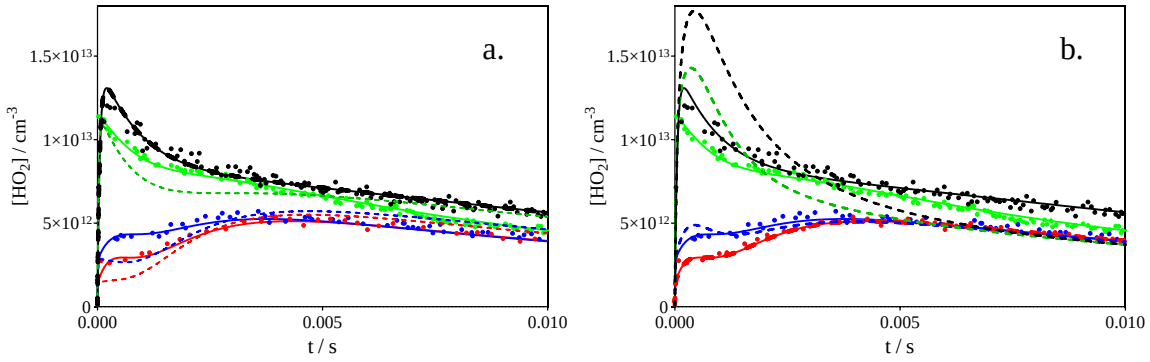

Figure 5: HO_2 absorption-time profiles from **Figure 4d**. Full lines with model from **Table 3**, Graph a. shows model without (21), but with k_{20} = 250 s^{-1}, reproducing very well the profile with the lowest $CH_3C(O)CH_3$ concentration, graph b. shows model with k_{20} = 3000 s^{-1}, reproducing very well the profile with the highest $CH_3C(O)CH_3$ concentration,

A reaction of Cl_2 with the Criegee intermediates, which has never been investigated, is probably also not involved in explaining the radical profiles: with the same Cl_2 concentration for all experiments such reaction would have in the Figure 4 experiments the same consequence as a unimolecular reaction and is therefore not a candidate for explaining the observed profiles. An upper limit for the rate constant of this reaction of 2.5×10^{-14} cm^3s^{-1} can be estimated from these experiments. Experiments focused on investigating the reaction of Criegee intermediates with Cl_2 through direct observation of the Criegee intermediate combined with theoretical calculations can be carried out to better understand this completely unknown class of reaction.

From this observation we have then considered a bi-molecular reaction of the Criegee intermediate with $CH_3C(O)CH_3$. The reaction has been studied several times [39-42] for the simplest Criegee intermediate, CH_2OO, and pressure dependent rate constants in the range 2.3×10^{-13} cm^3s^{-1} at 4 Torr He [39] up to a high pressure limit of 4.7×10^{-13} cm^3s^{-1} at 100 Torr N_2 [40] have been obtained. In our $CH_3C(O)CH_3$ concentration range, the high-pressure limit of the rate constant would result in pseudo-first order rate constants between 1800 – 34000 s^{-1}, i.e. much faster than the observed profiles. The reactivity of the more complex Criegee intermediate, $CH_3C(O)CHO_2$, has to our knowledge never been studied, but a lower reactivity can be expected[43] and therefore this reaction could be a candidate for explaining our observed HO_2 profiles. We have integrated into the model the reaction

$$CH_3C(O)CH_3 + CH_3C(O)CHO_2 \rightarrow\rightarrow HO_2 + \text{products} \qquad (21)$$

and the full lines in **Figure 5** show the model using $k_{21} = 4.5 \times 10^{-14}$ cm^3s^{-1}, *i.e.* one order of magnitude slower than the same reaction for the simplest Criegee. Excellent agreement for all HO_2 profiles over the full range of $CH_3C(O)CH_3$ concentration is obtained this way. We express by the double arrow that HO_2 formation does not occur in an elementary reaction, but in a reaction sequence. Addition of Criegee to $CH_3C(O)CH_3$ it a 1,3-bipolar cycloaddition which might lead to OH radicals, which in a subsequent rapid reaction with peroxy radicals could lead to HO_2 radicals. The given rate constant of (21) is therefore the rate-limiting step and the initial addition of $CH_3C(O)CHO_2$ to $CH_3C(O)CH_3$ might be faster. However, from the current experiments we cannot make the difference, and additional experiments, preferably with a direct detection of the Criegee intermediate, should be carried out to unravel the details of the HO_2 formation.

In **Figure 6** is shown again a series of experiments where (18) plays a role: the same low $CH_3C(O)CH_3$ concentration and the Cl-atom concentration varying between $(4.4 – 9.0) \times 10^{13}$ cm^{-3}, from purple to red. The full lines show the simulation corresponding to the model in **Table 3** and demonstrate the good performance of the implemented chemistry following the reaction of Cl-atoms with $CH_3C(O)CH_2O_2$. The dashed lines show the simulated profiles from **Table 3** without considering the reaction of Cl-atoms with $CH_3C(O)CH_2O_2$ radicals: the $CH_3C(O)CH_2O_2$ and the CH_3O_2 profiles are well reproduced and the reason for the disagreement could be searched for in some unexpected missing radical concentration. However, the HO_2 and the $CH_3C(O)O_2$ profiles cannot be reproduced without considering the reaction of Cl-atoms with $CH_3C(O)CH_2O_2$. Even for the lowest Cl-atom concentration the influence is clearly visible.

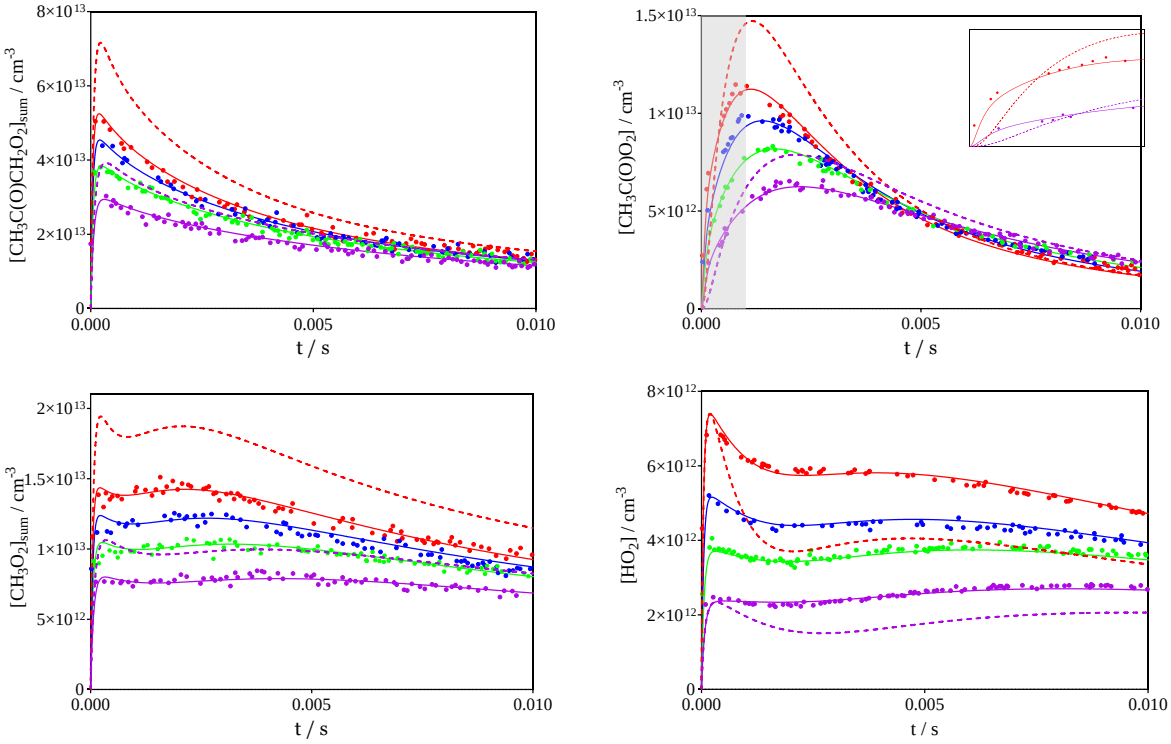

Figure 6: Concentration-time profiles for all 4 radicals: [Cl] = 9.0, 7.2, 6.0 and 4.4 × 10^{13} cm^{-3} for red, blue, green and purple symbols, respectively. [$CH_3C(O)CH_3$] = 7.0 × 10^{15} cm^{-3} for all experiments. Coloured lines are obtained using the model in **Table 3**, for CH_3O_2 and $CH_3C(O)CH_2O_2$ data points and full lines are expressed corresponding to (16) and (17), respectively. Dashed lines show modelled profiles without contribution of Cl + $CH_3C(O)CH_2O_2$ for the highest and lowest Cl-atom concentration.

Another possible bi-molecular reaction of the Criegee intermediate $CH_3C(O)CHO_2$ would be a reaction with peroxy radicals: this reaction has been investigated several times[44-47] and is known to lead to formation of OH radials. The OH radicals might then lead in subsequent reactions with peroxy radicals to HO_2[48-51]. This reaction sequence has tentatively been implemented into the model, but no rate constants could be found that resulted in satisfactorily results for all conditions. However, a minor participation of this reaction together with (21) cannot be excluded from the present results, separate experiments would be necessary to conclude on the detailed mechanism of the subsequent chemistry of $CH_3C(O)CHO_2$. Such experiments are out of the scope of this paper.

Self-reaction of $CH_3C(O)CH_2O_2$

Finally, the secondary Cl-atom chemistry presented in the model in **Table 3** allowed to very well reproduce the observed profiles under conditions where the reaction of Cl-atoms with peroxy radicals was favored. This mechanism has then been used to simulate experiments designed for measuring the rate constant of the self-reaction of $CH_3C(O)CH_2O_2$: high $CH_3C(O)CH_3$ concentrations, corresponding to the red symbols in **Figure 4** and **Figure 5**, have always been used in these experiments, conditions where (18) plays only a very minor role. The rate constants and branching ratios for the reaction of $CH_3C(O)CH_2O_2$ with $CH_3C(O)O_2$, CH_3O_2 and HO_2 are only poorly known[11-13] and the model in **Table 3** uses the current recommendations of the IUPAC committee[5].

Table 3: Full mechanism used to model the experimental data

No	Reaction	k / cm^3 s^{-1}	Ref.
Initial reactions			
3	$Cl + CH_3C(O)CH_3 \rightarrow CH_3C(O)CH_2 + HCl$	2.17×10^{-12}	32
4	$CH_3C(O)CH_2 + O_2 \rightarrow CH_3C(O)CH_2O_2$	1.2×10^{-12}	6
1a	$2\ CH_3C(O)CH_2O_2 \rightarrow$ stable products	2.2×10^{-12}	This work
1b	$2\ CH_3C(O)CH_2O_2 \rightarrow 2\ CH_3C(O)CH_2O + O_2 \rightarrow 2\ CH_3C(O) + 2\ CH_2O$	3.2×10^{-12}	This work
6a	$CH_3C(O) + O_2 \rightarrow CH_3C(O)O_2$	5.0×10^{-12}	5
6b	$CH_3C(O) + O_2 \rightarrow$ product + HO_2	1×10^{-13}	30
6c	$CH_3C(O) + O_2 \rightarrow$ product + OH	2×10^{-13}	30
Secondary peroxy radical chemistry			
7a	$CH_3C(O)CH_2O_2 + CH_3C(O)O_2 \rightarrow CH_3C(O)CH_2O + CH_3C(O)O + O_2$	2.5×10^{-12}	5
7b	$CH_3C(O)CH_2O_2 + CH_3C(O)O_2 \rightarrow$ stable products	2.5×10^{-12}	5
8a	$CH_3C(O)CH_2O_2 + CH_3O_2 \rightarrow CH_3C(O)CH_2O + CH_3O + O_2$	1.14×10^{-12}	5
8b	$CH_3C(O)CH_2O_2 + CH_3O_2 \rightarrow$ stable products	2.66×10^{-12}	5
9a	$CH_3C(O)CH_2O_2 + HO_2 \rightarrow CH_3C(O)CH_2O + OH + O_2$	1.35×10^{-12}	5
9b	$CH_3C(O)CH_2O_2 + HO_2 \rightarrow$ stable products	7.65×10^{-12}	5
10	$2\ CH_3C(O)O_2 \rightarrow 2\ CH_3C(O)O + O_2$	1.35×10^{-11}	21
11a	$CH_3C(O)O_2 + CH_3O_2 \rightarrow CH_3C(O)O + CH_3O + O_2$	1.35×10^{-11}	21
11b	$CH_3C(O)O_2 + CH_3O_2 \rightarrow$ stable products	7.05×10^{-12}	21
12a	$CH_3C(O)O_2 + HO_2 \rightarrow CH_3C(O)O + OH + O_2$	8×10^{-12}	52
12b	$CH_3C(O)O_2 + HO_2 \rightarrow$ stable products	8×10^{-12}	52
13a	$2\ CH_3O_2 \rightarrow 2\ CH_3O + O_2$	1.3×10^{-13}	5
13b	$2\ CH_3O_2 \rightarrow$ stable products	2.2×10^{-13}	5
14	$CH_3O_2 + HO_2 \rightarrow CH_3OOH + O_2$	5.5×10^{-12}	5

15	$2\ HO_2 \rightarrow H_2O_2 + O_2$	1.7×10^{-12}	[5]
22	$CH_3C(O)O \rightarrow CH_3 + CO_2$	$5.2 \times 10^{8}\ s^{-1}$	[53]
23	$CH_3O + O_2 \rightarrow CH_2O + HO_2$	1.9×10^{-15}	[5]
24	$CH_3O + HO_2 \rightarrow$ products	1.1×10^{-10}	[54]
25	$HO_2 + CH_3C(O)CH_3 \leftrightarrow CH_3C(O)CH_3 \bullet HO_2$	$K_c = 1.4 \times 10^{-18}$	[55]
Secondary Cl-atom chemistry			
18a	$Cl + CH_3C(O)CH_2O_2 \rightarrow CH_3C(O)CH_2O + ClO$	6×10^{-11}	This work
18b	$Cl + CH_3C(O)CH_2O_2 \rightarrow CH_3C(O)CHO_2 + HCl$	7.5×10^{-11}	This work
19	$Cl + CH_2O + O_2 \rightarrow HO_2 + CO + HCl$	7.3×10^{-11}	[5]
21	$CH_3C(O)CHO_2 + CH_3C(O)CH_3 \rightarrow\rightarrow HO_2 +$ products	4.5×10^{-14}	This work
OH chemistry			
26	$OH + CH_3C(O)CH_3 \rightarrow CH_3C(O)CH_2 + H_2O$	1.76×10^{-13}	[5]
27	$OH + CH_2O + O_2 \rightarrow HO_2 + CO + H_2O$	8.36×10^{-12}	[5]
28	$OH + CH_3C(O)CH_2O_2 \rightarrow CH_3C(O)CH_2OOOH$	1×10^{-10}	[49, 56]
29	$OH + CH_3O_2 \rightarrow CH_3O + HO_2$	1.2×10^{-12}	[17]

Figure 7 shows a series of experiments with high $CH_3C(O)CH_3$ concentration and Cl-atom concentration varying between 0.36 - 1.3 × 10^{14} cm^{-3}. The colored lines represent the simulation using the model from **Table 3**, and an excellent reproduction of the profiles of all four species is obtained over the entire Cl-concentration range.

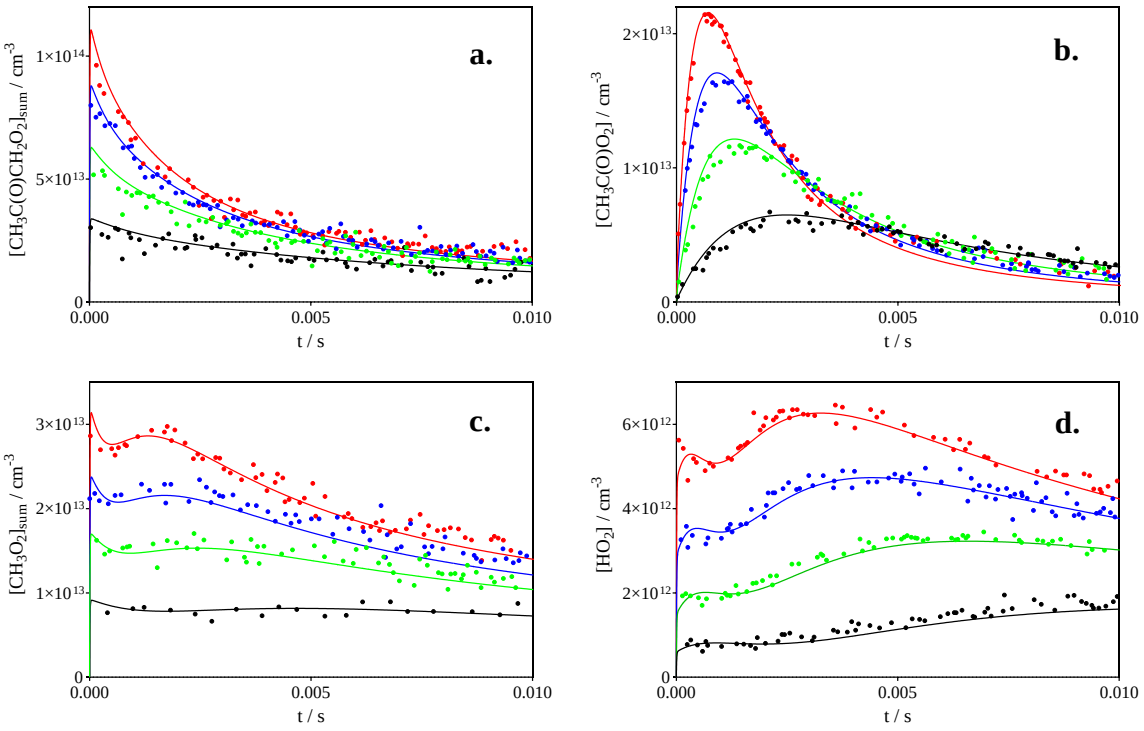

Figure 7: Absorption-time profiles for all 4 radicals: [Cl] = 1.3, 1.0, 0.69 and 0.36 × 10^{14} cm^{-3} for red, blue, green and black symbols, [$CH_3C(O)CH_3$] = 6.0 × 10^{16} cm^{-3} for all experiments. Coloured lines are obtained using the model in **Table 3**, for CH_3O_2 and $CH_3C(O)CH_2O_2$ data points and full lines are expressed corresponding to (16) and (17), respectively.

Figure 8 shows the profiles for the highest Cl-concentration from **Figure 7** (red symbols), but now all four species in one graph: $CH_3C(O)CH_2O_2$ (green, right y-axis applies), $CH_3C(O)O_2$ (blue), CH_3O_2 (black) and HO_2 (red). Different parameters have been varied compared to the model in **Table 3**:

- Graph a. shows again the best model from **Table 3** as full lines with a branching ratio of ϕ_{1b} = 0.6, while the dashed lines show the simulation with the same total rate constant k_1, but lower radical yield: ϕ_{1b} = 0.4, the dotted lines show the simulation with higher yield: ϕ_{1b} = 0.8. With the lower and the higher radical yield, the profile of $CH_3C(O)CH_2O_2$ is still reasonably well reproduced, but the concentrations of the three other radical species are clearly under/overestimated. From such simulations we estimate an uncertainty of the branching ratio of ± 0.1.
- Graph b. shows the sensitivity of the model to the overall rate constant k_1, while keeping ϕ_{1b} = 0.6: the dashed lines correspond to k_1 = 8.1 × 10^{-12} cm^3s^{-1}, i.e. an increase of 50%, the dotted lines represent the model with k_1 decreased by 50% (k_1 = 3.6 × 10^{-12} cm^3s^{-1}): none of these variations allows to reproduce all profiles. From such simulations we estimate an uncertainty of the rate constant k_1 of ±25%.

- Graph c. shows the simulation using the rate constant and branching ratio as currently recommended by IUPAC[5]: k_1 is slightly faster than the current value, but the branching ratio is very similar (see **Table 1**). The $CH_3C(O)CH_2O_2$ and CH_3O_2 profiles are well reproduced, however the $CH_3C(O)O_2$ concentration is overestimated at short reaction times, with (1b) being the major source of the $CH_3C(O)O_2$ radicals. This leads also to an overestimation of HO_2 which has its major source in the cross reaction between $CH_3C(O)O_2$ and CH_3O_2 radicals.
- Graph d. shows the simulation using the rate constant and branching ratio from Zuraski *et al.*[13]: while the rate constant is in excellent agreement with the current work, the branching ratio is with 0.33 much lower than our value. The resulting concentration-time profiles are much too low compared to the measurements. The reason for the very low branching ratio obtained by Zuraski *et al.* is possibly due to the fact that relatively low $CH_3C(O)CH_3$ (~2×10^{16} cm^{-3}, three times lower than typically used in this work) together with high Cl-atom concentrations (~1-2×10^{14} cm^{-3}) have been used in their experiments, conditions under which (18) plays a non-negligible role. However, no secondary Cl-atom chemistry has been integrated into their model, which certainly biased the results extracted from simulation of experimental radical profiles.

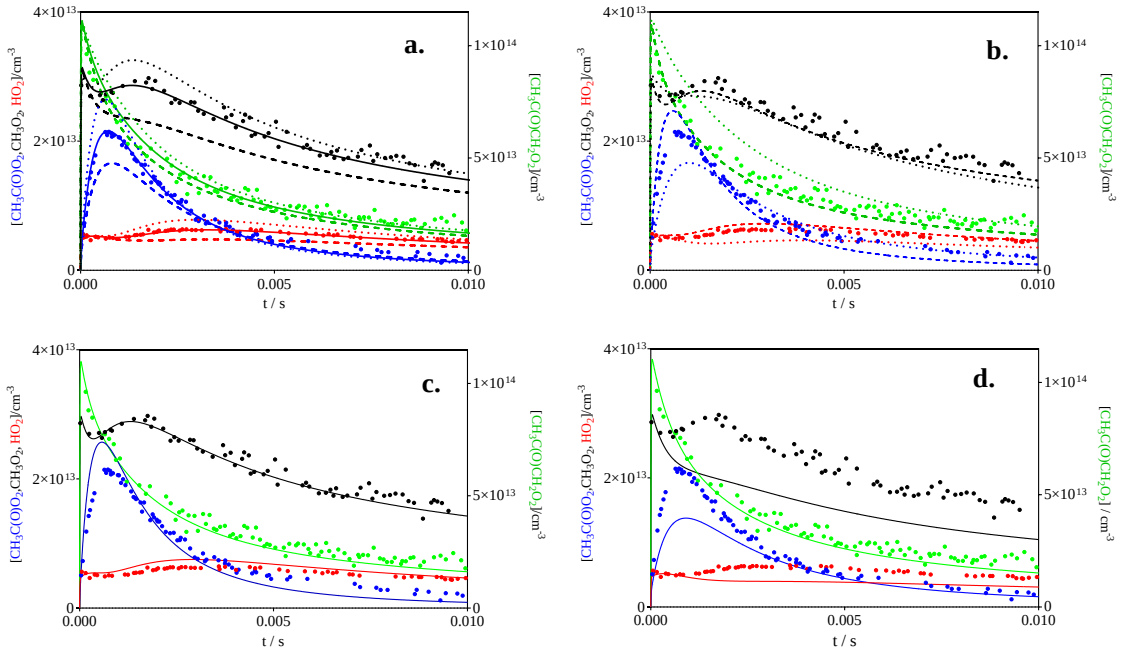

Figure 8: Absorption-time profiles for all 4 radicals ($CH_3C(O)CH_2O_2$ (green, right y-axis applies), $CH_3C(O)O_2$ (blue), CH_3O_2 (black) and HO_2 (red)) for the highest Cl-concentration from **Figure 7** ([Cl] = 1.3×10^{14} cm^{-3}, red symbols). Graph a: branching ratio for (1) is ϕ_{1b} = 0.6 (full lines, best model), 0.4 (dashed lines) and 0.8 (dotted lines). Graph b: dashed lines: k_1 = 8.1×10^{-12} cm^3s^{-1} (50% increase compared to best model), dotted lines: k_1 = 3.6×10^{-12} cm^3s^{-1} (50% decrease compared to best model). Graph c: current recommendation for k_1 and branching ratio from IUPAC committee. Graph d: model with rate constant and branching ratio for (1) from Zuraski *et al.*[13].

Conclusion

The rate constant and the branching ratio of the self-reaction of the acetonyl peroxy radical, $CH_3C(O)CH_2O_2$, has been determined. This is a complex reaction system, because one of the products of the self-reaction is the acetyl peroxy radical, $CH_3C(O)O_2$, which induces a rich, unavoidable secondary chemistry influencing the concentration-time profile of the $CH_3C(O)CH_2O_2$ radical. In this work, we present a selective detection of the four key species involved in the secondary chemistry of this system: cw-cavity ring down spectroscopy in the near infrared region. From modeling the concentration-time profiles of the four species (HO_2, CH_3O_2, $CH_3C(O)O_2$ and $CH_3C(O)CH_2O_2$), measured simultaneously in a large range of initial concentrations, a rate constant for the self-reaction of k_1 = (5.4 ± 1.4) × 10^{-12} cm^3s^{-1} has been obtained, in good agreement with a recent publication[13]. The branching ratio for the radical path however was found with ϕ_{1b} = (0.6 ± 0.1) well above the most recently published value (0.33 ± 0.13). This is a large disagreement, because the branching ratio of the radical path has a strong influence on the profiles of the different species and thus the agreement on the rate constant between both works, obtained with different branching ratios, must be fortuitous. It turned out that the reaction of Cl-atoms with $CH_3C(O)CH_2O_2$ is very fast, and can have an impact on the profiles, depending on the initial concentrations. Therefore, this reaction has been investigated in separate experiments with initial condition chosen to promote this reaction. A rate constant of k_{18} = (1.35 ± 0.8) × 10^{-10} cm^3s^{-1} was obtained by simultaneous modeling the concentration time profiles of all four radicals, and experimental results were best reproduced using a branching fraction of ϕ_{18b} = (0.55±0.1) leading through H-atom abstraction to the formation of the Criegee intermediate, $CH_3C(O)CHO_2$. In order to well reproduce the HO_2 profiles, a reaction of $CH_3C(O)CHO_2$ with the precursor acetone, $CH_3C(O)CH_3$, with a rate constant of k_{21} = (4.5 ± 2.0) × 10^{-14} cm^3s^{-1} needed to be added to the model. It is thought that this secondary Cl-atom chemistry is the reason for the disagreement in the branching ratio between this work and Zuraski *et al*.[13]

Supporting information

Figure S1: data from Figure 6 with different branching ratios for (18); Excel files containing all data presented in the figures (α = f(t) for all wavenumbers and all concentrations).

Acknowledgment

This project was supported by the French ANR agency under contract No. ANR-11-Labx-0005-01 CaPPA (Chemical and Physical Properties of the Atmosphere), the Région Hauts-de-France, the Ministère de l'Enseignement Supérieur et de la Recherche (CPER Climibio) and the European Fund for Regional Economic Development.

References

1. Khan, M. A. H.; Cooke, M. C.; Utembe, S. R.; Archibald, A. T.; Maxwell, P.; Morris, W. C.; Xiao, P.; Derwent, R. G.; Jenkin, M. E.; Percival, C. J*., et al.* A study of global atmospheric budget and distribution of acetone using global atmospheric model STOCHEM-CRI. *Atmos. Environ.* **2015,** *112*, 269-277
2. Elias, T.; Szopa, S.; Zahn, A.; Schuck, T.; Brenninkmeijer, C.; Sprung, D.; Slemr, F. Acetone variability in the upper troposphere: analysis of CARIBIC observations and LMDz-INCA chemistry-climate model simulations. *Atmos. Chem. Phys.* **2011,** *11*, 8053-8074
3. Franco, B.; Clarisse, L.; Stavrakou, T.; Müller, J. F.; Pozzer, A.; Hadji-Lazaro, J.; Hurtmans, D.; Clerbaux, C.; Coheur, P. F. Acetone Atmospheric Distribution Retrieved From Space. *Geophysical Research Letters* **2019,** *46*, 2884−2893
4. Fischer, E. V.; Jacob, D. J.; Millet, D. B.; Yantosca, R. M.; Mao, J. The role of the ocean in the global atmospheric budget of acetone. *Geophysical research letters* **2012,** *39*, 10.1029/2011gl050086
5. Atkinson, R.; Baulch, D. L.; Cox, R. A.; Crowley, J. N.; Hampson, R. F.; Hynes, R. G.; Jenkin, M. E.; M. J. Rossi; Troe, J. Evaluated Kinetic and Photochemical Data for Atmospheric Chemistry: Volume II - Gas Phase Reactions of Organic Species. *Atmos. Chem. Phys.* **2006,** *6*, 3625-4055
6. Hassouna, M.; Delbos, E.; Devolder, P.; Viskolcz, B.; Fittschen, C. Rate and Equilibrium Constant of the Reaction of 1-Methylvinoxy Radicals with O_2: $CH_3COCH_2 + O_2 \leftrightarrow CH_3COCH_2O_2$. *J. Phys. Chem. A* **2006,** *110*, 6667-6672
7. Delbos, E.; Fittschen, C.; Hippler, H.; Krasteva, N.; Olzmann, M.; Viskolcz, B. Rate Coefficients and Equilibrium Constant for the $CH_2CHO + O_2$ Reaction System. *J. Phys. Chem. A* **2006,** *110*, 3238-3245
8. Sehested, J.; Christensen, L. K.; Nielsen, O. J.; Bilde, M.; Wallington, T. J.; Schneider, W. F.; Orlando, J. J.; Tyndall, G. S. Atmospheric chemistry of acetone: Kinetic study of the $CH_3C(O)CH_2O_2$+NO/NO_2 reactions and decomposition of $CH_3C(O)CH_2O_2NO_2$. *Int. J. Chem. Kinet.* **1998,** *30*, 475-489
9. Orlando, J. J.; Tyndall, G. S.; Vereecken, L.; Peeters, J. The Atmospheric Chemistry of the Acetonoxy Radical. *J. Phys. Chem. A* **2000,** *104*, 11578-11588
10. Orlando, J. J.; Tyndall, G. S. Laboratory studies of organic peroxy radical chemistry: an overview with emphasis on recent issues of atmospheric significance. *Chem. Soc. Rev.* **2012,** *41*, 6294-317
11. Bridier, I.; Veyret, B.; Lesclaux, R.; Jenkin, M. E. Flash photolysis study of the UV spectrum and kinetics of reactions of the acetonylperoxy radical. *J. Chem. Soc., Faraday Trans.* **1993,** *89*, 2993 - 2997
12. Jenkin, M. E.; Cox, R. A.; Emrich, M.; Moortgat, G. K. Mechanisms of the Cl-atom-initiated oxidation of acetone and hydroxyacetone in air. *J. Chem. Soc., Faraday Trans.* **1993,** *89*, 2983-2991

13. Zuraski, K.; Hui, A. O.; Grieman, F. J.; Darby, E.; Møller, K. H.; Winiberg, F. A. F.; Percival, C. J.; Smarte, M. D.; Okumura, M.; Kjaergaard, H. G.*, et al.* Acetonyl Peroxy and Hydro Peroxy Self- and Cross-Reactions: Kinetics, Mechanism, and Chaperone Enhancement from the Perspective of the Hydroxyl Radical Product. *J. Phys. Chem. A* **2020,** *124*, 8128-8143
14. Cox, R. A.; Munk, J.; Nielsen, O. J.; Pagsberg, P.; Ratajczak, E. Ultraviolet absorption spectra and kinetics of acetonyl and acetonylperoxy radicals. *Chem. Phys. Lett.* **1990,** *173*, 206-210
15. Emrich, M.; Warneck, P. Branching Ratio For The Self-Reaction Of Acetonyl Peroxy Radicals. *Zeitschrift für Naturforschung A* **2003,** *58*, 429-433
16. Berndt, T.; Scholz, W.; Mentler, B.; Fischer, L.; Herrmann, H.; Kulmala, M.; Hansel, A. Accretion Product Formation from Self- and Cross-Reactions of RO_2 Radicals in the Atmosphere. *Angew. Chem. Int. Ed.* **2018,** *57*, 3820-3824
17. Assaf, E.; Song, B.; Tomas, A.; Schoemaecker, C.; Fittschen, C. Rate Constant of the Reaction between CH_3O_2 Radicals and OH Radicals revisited. *J. Phys. Chem. A* **2016,** *120*, 8923-8932
18. Votava, O.; Masat, M.; Parker, A. E.; Jain, C.; Fittschen, C. Microcontroller Based Resonance Tracking unit for Time Resolved Continuous wave Cavity-Ringdown Spectroscopy Measurements. *Rev. Sci. Instrum.* **2012,** *83*, 043110
19. Parker, A.; Jain, C.; Schoemaecker, C.; Szriftgiser, P.; Votava, O.; Fittschen, C. Simultaneous, Time-Resolved Measurements of OH and HO_2 Radicals by Coupling of High Repetition Rate LIF and cw-CRDS Techniques to a Laser Photolysis Reactor and its Application to the Photolysis of H_2O_2 *Appl. Phys. B* **2011,** *103*, 725-733
20. Morajkar, P.; Bossolasco, A.; Schoemaecker, C.; Fittschen, C. Photolysis of CH_3CHO at 248 nm: Evidence of Triple Fragmentation from Primary Quantum Yield of CH_3 and HCO Radicals and H Atoms. *J. Chem. Phys.* **2014,** *140*, 214308
21. Assali, M.; Fittschen, C. Rate Constants and Branching Ratios for the Self-Reaction of Acetyl Peroxy ($CH_3C(O)O_2$) and Its Reaction with CH_3O_2. *Atmosphere* **2022,** *13*, 186
22. Devolder, P.; Dusanter, S.; Lemoine, B.; Fittschen, C. About the Co-Product of the OH Radical in the Reaction of Acetyl with O_2 below Atmospheric Pressure. *Chem. Phys. Lett.* **2006,** *417*, 154-158
23. Thiebaud, J.; Crunaire, S.; Fittschen, C. Measurement of Line Strengths in the $2\nu_1$ Band of the HO_2 Radical using Laser Photolysis / Continous wave Cavity Ring Down Spectroscopy (cw-CRDS). *J. Phys. Chem. A* **2007,** *111*, 6959-6966
24. Ibrahim, N.; Thiebaud, J.; Orphal, J.; Fittschen, C. Air-Broadening Coefficients of the HO_2 Radical in the $2\nu_1$ Band Measured Using cw-CRDS. *J. Mol. Spectrosc.* **2007,** *242*, 64-69
25. Assaf, E.; Asvany, O.; Votava, O.; Batut, S.; Schoemaecker, C.; Fittschen, C. Measurement of line strengths in the $\tilde{A}\ ^2A' \leftarrow X\ ^2A''$ transition of HO_2 and DO_2. *J. Quant. Spectrosc. Radiat. Transfer* **2017,** *201*, 161-170
26. Assaf, E.; Liu, L.; Schoemaecker, C.; Fittschen, C. Absorption spectrum and absorption cross sections of the $2\nu_1$ band of HO_2 between 20 and 760 Torr air in the range 6636 and 6639 cm^{-1}. *Journal of Quantitative Spectroscopy & Radiative Transfer* **2018,** *211*, 107-114
27. DeSain, J. D.; Ho, A. D.; Taatjes, C. A. High-resolution diode laser absorption spectroscopy of the O–H stretch overtone band (2,0,0)(0,0,0) of the HO_2 radical. *J. Mol. Spectrosc.* **2003,** *219*, 163-169
28. Onel, L.; Brennan, A.; Gianella, M.; Ronnie, G.; Lawry Aguila, A.; Hancock, G.; Whalley, L.; Seakins, P. W.; Ritchie, G. A. D.; Heard, D. E. An intercomparison of HO_2 measurements by Fluorescence Assay by Gas Expansion and Cavity Ring–Down Spectroscopy within HIRAC (Highly Instrumented Reactor for Atmospheric Chemistry). *Atmos. Meas. Tech. Discuss.* **2017,** *10*, 4877-4894
29. Tang, Y.; Tyndall, G. S.; Orlando, J. J. Spectroscopic and Kinetic Properties of HO_2 Radicals and the Enhancement of the HO_2 Self Reaction by CH_3OH and H_2O. *J. Phys. Chem. A* **2010,** *114*, 369-378
30. Rolletter, M.; Assaf, E.; Assali, M.; Fuchs, H.; Fittschen, C. The absorption spectrum and absolute absorption cross sections of acetylperoxy radicals, $CH_3C(O)O_2$ in the near IR. *J. Quant. Spectrosc. Radiat. Transfer* **2020,** *245*, 106877
31. Faragó, E. P.; Viskolcz, B.; Schoemaecker, C.; Fittschen, C. Absorption Spectrum and Absolute Absorption Cross Sections of CH_3O_2 Radicals and CH_3I Molecules in the Wavelength Range 7473–7497 cm^{-1}. *J. Phys. Chem. A* **2013,** *117*, 12802-12811

32. Romanias, M. N.; Stefanopoulos, V. G.; Papanastasiou, D. K.; Papadimitriou, V. C.; Papagiannakopoulos, P. Temperature-dependent rate coefficients and mechanism for the gas-phase reaction of chlorine atoms with acetone. *Int. J. Chem. Kinet.* **2010,** *42*, 724-734
33. Daele, V.; Poulet, G. Kinetics and products of the reactions of CH_3O_2 with Cl and ClO. *Journal de Chimie Physique* **1996,** *93*, 1081-1099
34. Maricq, M. M.; Szente, J. J.; Kaiser, E. W.; Shi, J. Reaction of Chlorine Atoms with Methylperoxy and Ethylperoxy Radicals. *J. Phys. Chem.* **1994,** *98*, 2083-2089
35. Drougas, E.; Kosmas, A. M. Quantum mechanical studies on the potential energy surface of the reactions CH_3+OClO, CH_3O+ClO and CH_3O_2+Cl. *Chem. Phys. Lett.* **2003,** *369*, 269-274
36. Morajkar, P.; Schoemaecker, C.; Okumura, M.; Fittschen, C. Direct Measurement of the Equilibrium Constants of the Reaction of Formaldehyde and Acetaldehyde with HO_2 Radicals. *Int. J. Chem. Kinet.* **2014,** *46*, 245–259
37. Vereecken, L.; Novelli, A.; Taraborrelli, D. Unimolecular decay strongly limits the atmospheric impact of Criegee intermediates. *Phys. Chem. Chem. Phys.* **2017,** *19*, 31599-31612
38. Vereecken, L.; Novelli, A.; Kiendler-Scharr, A.; Wahner, A. Unimolecular and water reactions of oxygenated and unsaturated Criegee intermediates under atmospheric conditions. *Phys. Chem. Chem. Phys.* **2022,** *24*, 6428-6443
39. Taatjes, C. A.; Welz, O.; Eskola, A. J.; Savee, J. D.; Osborn, D. L.; Lee, E. P. F.; Dyke, J. M.; Mok, D. W. K.; Shallcross, D. E.; Percival, C. J. Direct measurement of Criegee intermediate (CH_2OO) reactions with acetone, acetaldehyde, and hexafluoroacetone. *Phys. Chem. Chem. Phys.* **2012,** *14*, 10391-10400
40. Chhantyal-Pun, R.; Khan, M. A. H.; Martin, R.; Zachhuber, N.; Buras, Z. J.; Percival, C. J.; Shallcross, D. E.; Orr-Ewing, A. J. Direct Kinetic and Atmospheric Modeling Studies of Criegee Intermediate Reactions with Acetone. *ACS Earth and Space Chemistry* **2019,** *3*, 2363-2371
41. Cornwell, Z. A.; Harrison, A. W.; Murray, C. Kinetics of the Reactions of CH_2OO with Acetone, alpha-Diketones, and beta-Diketones. *J. Phys. Chem. A* **2021,** *125*, 8557-8571
42. Elsamra, R. M. I.; Jalan, A.; Buras, Z. J.; Middaugh, J. E.; Green, W. H. Temperature- and Pressure-Dependent Kinetics of CH_2OO + CH_3COCH_3 and CH_2OO + CH_3CHO: Direct Measurements and Theoretical Analysis. *Int. J. Chem. Kinet.* **2016,** *48*, 474-488
43. Vereecken, L.; Harder, H.; Novelli, A. The reactions of Criegee intermediates with alkenes, ozone, and carbonyl oxides. *Phys. Chem. Chem. Phys.* **2014,** *16*, 4039-4049
44. Chhantyal-Pun, R.; Khan, M. A. H.; Zachhuber, N.; Percival, C. J.; Shallcross, D. E.; Orr-Ewing, A. J. Impact of Criegee Intermediate Reactions with Peroxy Radicals on Tropospheric Organic Aerosol. *ACS Earth and Space Chemistry* **2020,** *4*, 1743-1755
45. Vereecken, L.; Harder, H.; Novelli, A. The reaction of Criegee intermediates with NO, RO2, and SO2, and their fate in the atmosphere. *Phys. Chem. Chem. Phys.* **2012,** *14*, 14682-14695
46. Zhao, Q.; Wang, W.; Liu, F.; Lü, J.; Wang, W. Oligomerization reactions for precursors to secondary organic aerosol: Comparison between two formation mechanisms for the oligomeric hydroxyalkyl hydroperoxides. *Atmos. Environ.* **2017,** *166*, 1-8
47. Zhao, Q.; Liu, F.; Wang, W.; Li, C.; Lü, J.; Wang, W. Reactions between hydroxyl-substituted alkylperoxy radicals and Criegee intermediates: correlations of the electronic characteristics of methyl substituents and the reactivity. *Phys. Chem. Chem. Phys.* **2017,** *19*, 15073-15083
48. Fittschen, C. The reaction of peroxy radicals with OH radicals. *Chem. Phys. Lett.* **2019,** *725*, 102-108
49. Assaf, E.; Schoemaecker, C.; Vereecken, L.; Fittschen, C. Experimental and Theoretical Investigation of the Reaction of RO_2 Radicals with OH Radicals: Dependence of the HO_2 Yield on the Size of the Alkyl Group. *Int. J. Chem. Kinet.* **2018,** *50*, 670–680
50. Assaf, E.; Sheps, L.; Whalley, L.; Heard, D.; Tomas, A.; Schoemaecker, C.; Fittschen, C. The Reaction between CH_3O_2 and OH Radicals: Product Yields and Atmospheric Implications. *Environ. Sci. Technol.* **2017,** *51*, 2170-2177
51. Assaf, E.; Tanaka, S.; Kajii, Y.; Schoemaecker, C.; Fittschen, C. Rate constants of the reaction of C_2–C_4 peroxy radicals with OH radicals. *Chem. Phys. Lett.* **2017,** *684*, 245-249

52. Hui, A. O.; Fradet, M.; Okumura, M.; Sander, S. P. Temperature Dependence Study of the Kinetics and Product Yields of the HO_2 + $CH_3C(O)O_2$ Reaction by Direct Detection of OH and HO_2 Radicals Using 2f-IR Wavelength Modulation Spectroscopy. *J. Phys. Chem. A* **2019,** *123*, 3655-3671
53. Zhou, Y. Z.; Li, S.; Li, Q. S.; Zhang, S. W. Theoretical investigation of the decarboxylation reaction of CH_3CO_2 radical. *Journal of Molecular Structure: THEOCHEM* **2008,** *854*, 40-45
54. Assaf, E.; Schoemaecker, C.; Vereecken, L.; Fittschen, C. The reaction of fluorine atoms with methanol: yield of CH_3O/CH_2OH and rate constant of the reactions CH_3O + CH_3O and CH_3O + HO_2. *Phys. Chem. Chem. Phys.* **2018,** *20*, 8707
55. Burkholder, J. B.; Sander, S. P.; Abbatt, J. P. D.; Barker, J. R.; C., C.; J.D., C.; T.S., D.; Huie, R. E.; Kolb, C. E.; Kurylo, M. J.*, et al.*, *Chemical Kinetics and Photochemical Data for Use in Atmospheric Studies, Evaluation No. 19, JPL Publication 19-5*. 2020.
56. Fittschen, C.; Al Ajami, M.; Batut, S.; Ferracci, V.; Archer-Nicholls, S.; Archibald, A. T.; Schoemaecker, C. ROOOH: a missing piece of the puzzle for OH measurements in low-NO environments? *Atmos. Chem. Phys.* **2019,** *19*, 349-362